

# An explainable operator approximation framework under the guideline of Green's function

Jianghang Gu<sup>a,b</sup>, Ling Wen<sup>a</sup>, Yuntian Chen<sup>\*b,c</sup>, Shiyi Chen<sup>\*\*a,b,c</sup>

<sup>a</sup>State Key Laboratory of Turbulence and Complex Systems, College of Engineering, Peking University, Beijing, 100871, P. R. China

<sup>b</sup>Ningbo Institute of Digital Twin, Eastern Institute of Technology, Ningbo, 315200, Zhejiang, P. R. China

<sup>c</sup>Zhejiang Key Laboratory of Industrial Intelligence and Digital Twin, Eastern Institute of Technology, Ningbo, 315200, Zhejiang, P. R. China

---

## Abstract

Traditional numerical methods, such as the finite element method and finite volume method, address partial differential equations (PDEs) by discretizing them into algebraic equations and solving these iteratively. However, this process is often computationally expensive and time-consuming. An alternative approach involves transforming PDEs into integral equations and solving them using Green's functions, which provide analytical solutions. Nevertheless, deriving Green's functions analytically is a challenging and non-trivial task, particularly for complex systems. In this study, we introduce a novel framework, termed GreensONet, which is constructed based on the structure of deep operator networks (DeepONet) to learn embedded Green's functions and solve PDEs via Green's integral formulation. Specifically, the Trunk Net within GreensONet is designed to approximate the unknown Green's functions of the system, while the Branch Net are utilized to approximate the auxiliary gradients of the Green's function. These outputs are subsequently employed to perform surface integrals and volume integrals, incorporating user-defined boundary conditions and source terms, respectively. The effectiveness of the proposed framework is demonstrated on three types of PDEs in bounded domains: 3D heat conduction equations, reaction-diffusion equations, and Stokes equations. Comparative results in these cases demonstrate that GreenONet's accuracy and generalization ability surpass those of existing methods, including Physics-Informed Neural Networks (PINN), DeepONet, Physics-Informed DeepONet (PI-DeepONet), and Fourier Neural Operators (FNO). Code and data is available at <https://github.com/hangjianggu/GreensONet>.

**Keywords:** Green's function, Operator approximation, Integral solutions

---

## 1. Introduction

In recent years, the applications of deep learning to solve partial differential equations (PDEs) have garnered significant attention [1], offering promising alternatives to traditional numerical methods such as finite difference methods [2], finite element methods [3], and finite volume methods [4]. Unlike these conventional techniques, which often struggle with complex geometries and high computational expense, deep learning approaches have demonstrated the ability to efficiently solve PDEs over irregular domains [5, 6, 7, 8]. This capability has spurred interest across a wide range of fields, including fluid dynamics [9, 10, 11], elasticity [12], seismology [13], and beyond [14], where the need for fast, accurate, and scalable solutions to complex physical problems is critical. By leveraging data-driven models, deep learning techniques not only accelerate computation but also enable more flexible and adaptive solutions, especially for problems involving intricate and high-dimensional domains.

Prominent deep learning methods for solving PDEs can be broadly categorized into three approaches: (1) learning the solution to the PDEs directly [15, 16, 17], (2) learning the operators that define the underlying physics [6, 18, 19], and (3) learning the operators with PDE-based loss constraints [8, 20, 21]. Each approach offers distinct advantages and limitations, tailored to specific problem settings. The first approach focuses on approximating the solution to

---

\*ychen@eitech.edu.cn

\*\*chensy@sustech.edu.cn

the PDEs by directly minimizing the residual of the governing equations. A notable example is physics-informed neural networks (PINNs) [16], which embed the PDEs into the loss function of the neural network. This method effectively enforces physical laws without requiring labeled data but can struggle with convergence in complex or high-dimensional problems. The second approach shifts focus to learning the differential operators that describe the underlying physics. Methods such as Fourier Neural Operators (FNO) [18] and Deep Operator Networks (DeepONet) [6] aim to approximate the operator mapping input parameters to solutions for a family of PDEs. These methods enable efficient predictions for new parameters within the training range, but their accuracy may degrade for out-of-distribution parameters or complex domains. The third approach combines elements of the first two, integrating operator learning with physics-based constraints. For example, physics-informed DeepONet (PI-DeepONet) [8] leverages the strengths of PINN and DeepONet by simultaneously learning the operator and minimizing the PDEs residual. This hybrid approach improves generalization over parameter families while retaining physical consistency. However, it often requires significant computational resources due to the combined loss constraints. The following sections will provide a detailed examination of these approaches, highlighting their development, advantages, and limitations, and identifying opportunities for further improvement in PDEs-solving frameworks.

Physics-informed deep learning approaches approximate the solutions to PDEs along with their boundary and initial conditions by minimizing the residuals of the PDEs, leveraging automatic differentiation. Unlike data-driven methods, physics-informed deep learning does not require pre-existing datasets, making it particularly advantageous in scenarios where experimental or numerical data collection is expensive or time-consuming. The predominant framework in physics-informed deep learning employs a least-squares approach, where the loss function is defined using the  $L^2$ -norm of the strong form residual [16]. For problems with limited solution regularity, alternative formulations can be adopted. For instance, in symmetric problems, the loss function may be defined by minimizing the energy potential, as in the Ritz formulation [17]. Similarly, the norm of the residual functional can be minimized in a weak formulation, as demonstrated in works such as [15, 22]. To improve the training efficiency and accuracy of PINN, researchers have proposed several enhancement techniques. Among these, domain decomposition methods have proven particularly effective. Noteworthy implementations include conservative PINN [23], extended PINN [24], and finite basis PINN [25], which partition the solution domain into subdomains, each modeled by an independent neural network. This decomposition facilitates the application of PINN to large-scale and complex real-world problems. In addition, optimization algorithms with adaptive weighting strategies have been introduced to address convergence challenges in PINN training. For example, Wang et al. [26] proposed an algorithm where the loss weights for PDEs and boundary conditions are dynamically computed using the eigenvalues of the neural tangent kernel matrix at each iteration. To overcome spectral bias [27] and enhance the network’s ability to capture high-frequency components, Fourier feature mappings have also been incorporated into PINN architectures [28]. In [29], Xu et al. provides a weight-adjusting strategy in training process of PINN by increasing the weights of rules with positive importance and decreasing the weights of rules with negative importance. Despite these advancements, the application of PINN to high-dimensional problems remains hindered by slow convergence and accuracy degradation, particularly when recalculations are required for new forcing terms or boundary conditions. Addressing these challenges is critical for advancing the robustness and scalability of PINN in real-world applications.

In operator learning methods, the performance of neural networks is heavily influenced by the quality and diversity of the training dataset. Models such as DeepONet [6] and FNO [18] rely on well-curated datasets to achieve accurate operator approximations. DeepONet, designed to learn mappings between function spaces, requires a dataset that comprehensively captures the underlying functional relationships. Similarly, FNO, which employs Fourier transforms to parameterize neural networks, depends on high-quality data that accurately reflects the spectral characteristics of the problem domain. The Laplace Neural Operator [30] introduces an innovative approach by utilizing the Laplace transform to decompose the input space. This enables it to handle non-periodic signals and transient responses effectively while achieving exponential convergence and improved generalization. In another advancement, Koopman operator learning [31] leverages the Coupling Flow Invertible Neural Network (CF-INN) framework to learn invariant subspaces of the Koopman operator. By utilizing CF-INN’s invertibility, this method circumvents the challenge of manually selecting observable functions and facilitates accurate reconstruction of state variables. Transolver [32] represents a further refinement in operator learning methods. It introduces a novel Physics-Attention mechanism that adaptively partitions discretized domains into learnable slices based on intrinsic physical states. By capturing intricate physical correlations across complex geometries, Transolver outperforms existing approaches, setting a new benchmark in modeling complex PDEs. These examples underscore the importance of constructing a high-quality,

representative training dataset to ensure robust performance and generalization in operator learning. Consequently, meticulous attention to data preprocessing, augmentation, and selection is indispensable. Although training such neural networks can be computationally expensive, it needs to be performed only once. During the online phase, computing the solution for new parameter values involves a single forward pass, making this approach cost-effective for problems requiring solutions across a wide range of parameters. However, a notable limitation of operator learning methods lies in their lack of interpretability, which restricts their broader applicability despite their computational efficiency.

In addition to PINN-based and operator learning approaches, a third paradigm has emerged that integrates the strengths of PINN and DeepONet. Notably, PI-DeepONet [8] enhance the traditional DeepONet framework by embedding information from governing equations, resulting in improved predictive accuracy and more efficient data utilization. For instance, a Multi-Branch PI-DeepONet has been employed in [20, 21] to perform thermal simulations for predefined parameters, including heat sources, loads, boundary conditions, and initial conditions. Similarly, PI-DeepONet has demonstrated its effectiveness in solving both forward and inverse PDEs problems on unknown manifolds [33], providing accurate approximations comparable to those obtained by more computationally expensive methods that directly solve the PDEs with the proposed diffusion coefficient. Furthermore, a discretization-independent parameter embedding was introduced into PI-DeepONet [34] to enhance its expressive capacity, particularly for problems defined on irregular domains. This hybrid methodology effectively combines the interpretability of PINN with the computational efficiency of operator learning, enabling rapid and accurate predictions across diverse parameter spaces while retaining the physical insights offered by the governing equations. However, the incorporation of physical loss calculations across a batch of samples results in higher computational costs.

The primary objective of this paper is to develop an explainable operator approximation framework with lower training costs compared to PI-DeepONet. Central to the framework is the direct approximation of the Green’s function for PDE systems, enabling solutions to be obtained via integration. This approach has provided clear physical interpretability, guaranteed generalization performance, and its utility in analyzing the well-posedness and regularity properties of PDEs. Building on this motivation, several similar techniques based on the approximation of the Green’s function have been recently considered for the solution of linear and non-linear operators, see e.g. [19, 35, 36, 37, 38]. Specifically, the authors in [19] introduced the graph neural operator, which is inspired by the Green’s function. In [35], a dual-autoencoder architecture is presented to approximate the operator for non-linear boundary value problems, by linearizing the problem and approximating the corresponding Green’s function. Nevertheless, the linear integral operator is also given by the neural network, which introduces redundancy and compromises accuracy. Boulle et al. [36] tackled PDE problems by decomposing them into two components: one with homogeneous boundary conditions and the other with non-homogeneous boundary conditions. They employed two separate rational neural networks [39] to approximate the Green’s function influenced by force terms and the homogeneous solution influenced by boundary conditions, respectively. However, this approach requires retraining the networks whenever boundary conditions change, limiting its flexibility. Teng et al. [37] proposed an unsupervised method, akin to PINN, to learn the Green’s functions for linear reaction-diffusion equations with Dirichlet boundary conditions. Their approach approximates the Dirac delta function with a Gaussian density function. Building on this, Negi et al. [40] used a radial basis function (RBF) kernel-based neural network to better adapt to the singularity of the Dirac delta function. While these methods improve the approximation of Green’s functions, the use of surrogate functions like Gaussian or RBF kernels imposes limitations on accuracy, ultimately affecting the precision of the PDE solutions. Another line of data-free framework for learning Green’s functions was proposed in [38], relying solely on PDE constraints for training. While this approach enhances reliability by eliminating dependence on labeled data, it is primarily suited for lower-dimensional problems, limiting its scalability to higher-dimensional or more complex domains. In conclusion, these methods demonstrate significant progress in using neural networks to approximate Green’s functions and provide efficient solutions for PDEs. However, they lack a boundary-invariant and source-term-invariant framework that is sufficiently flexible to handle complex 3D bounded domains. This limitation highlights the need for a more generalized and robust approach to address these challenges effectively.

To address the limitations of existing Green’s function approximation frameworks, we propose a general and flexible Green’s function approximation framework based on the structure of DeepONet, referred to as **GreensONet**. DeepONet serves as the backbone for our framework due to its versatility, as it does not rely on prior knowledge of the solution structure and can be readily applied to a wide range of problems. In GreensONet, the Trunk Net is designed to approximate the unknown Green’s functions of the system, while the Branch Net are employed to es-

timate the auxiliary gradients of the Green’s function. These outputs are then used to perform surface and volume integrals, incorporating user-defined boundary conditions and source terms. By minimizing the deviation between the solutions derived from the acquired Green’s functions and the exact solutions, the framework effectively tunes the Green’s function for accurate approximation. To further enhance the capability of the trunk and Branch Net in capturing the singularities of Green’s functions, we introduce a novel binary-structured neural network architecture within these components. This design improves the accuracy and robustness of the approximations. GreensONet supports flexible geometric inputs, such as meshes or scattered data points, and accommodates versatile boundary conditions, source terms, and different types of equations, including heat conduction equations and reaction-diffusion equations. Furthermore, it extends to multi-physics simulations, such as Stokes equations. Our experiments demonstrate that GreensONet consistently outperforms state-of-the-art methods, including PINN, DeepONet, PI-DeepONet, and FNO, across several classical 3D PDE benchmark cases, showcasing its superior performance and broad applicability.

Our contributions are summarized as follows:

- We propose a novel Green’s function-based deep learning framework capable of learning boundary-invariant and source-term invariant Green’s functions on 3D bounded domains.
- We design a flexible framework that supports diverse geometric input formats, versatile boundary conditions and source terms, and computations for PDEs with both homogeneous and heterogeneous coefficients.
- We introduce a binary-structured neural network to effectively capture the singularities of Green’s functions.

This paper is organized into four sections. In Section 2, we present the fundamental mathematical theorems as preliminaries. Section 3 introduces the GreensONet framework. In Section 4, we present numerical results and validations. Finally, conclusions and outlooks are provided in Section 5.

## 2. Preliminaries

We introduce here some preliminaries and notations in order to describe the notion of the operators in PDEs. We first present the model problem and continue with a brief account of Green’s functions to solve boundary-value problems. Based on these foundations, we outline the core approach of our framework.

Let  $\Omega \subset \mathbb{R}^d$  be a bounded domain, we consider the linear PDE operator with Dirichlet boundary condition of the following form:

$$\begin{cases} \mathcal{L}(u)(\mathbf{x}) = f(\mathbf{x}), & \mathbf{x} \in \Omega \\ u(\mathbf{x}) = g(\mathbf{x}), & \mathbf{x} \in \partial\Omega \end{cases} \quad (1)$$

where  $f(\mathbf{x})$  is the given source term,  $g(\mathbf{x})$  is the boundary value.

The Green’s function  $G(\mathbf{x}, \boldsymbol{\xi})$  represents the impulse response of the PDE subject to homogeneous Dirichlet boundary condition, that is, for any impulse source point  $\boldsymbol{\xi} \in \Omega$ ,

$$\begin{cases} \mathcal{L}(G)(\mathbf{x}, \boldsymbol{\xi}) = \delta(\mathbf{x} - \boldsymbol{\xi}), & \mathbf{x} \in \Omega \\ G(\mathbf{x}, \boldsymbol{\xi}) = 0, & \mathbf{x} \in \partial\Omega \end{cases} \quad (2)$$

where  $\delta(\mathbf{x})$  denotes the Dirac delta source function satisfying  $\delta(\mathbf{x}) = 0$  if  $\mathbf{x} \neq 0$  and  $\int_{\mathbb{R}^d} \delta(\mathbf{x}) d\mathbf{x} = 1$ .

It is important to note that the Green’s function  $G(\mathbf{x}, \boldsymbol{\xi})$  satisfies Eq. (2) independently of the specific boundary conditions and force term in Eq. (1). If  $G(\mathbf{x}, \boldsymbol{\xi})$  in Eq. (2) is known, the solution to the problem defined by Eq. (1) can be directly computed using the following formula, which accommodates both variable boundary conditions and source terms:

$$u(\mathbf{x}) = \int_{\Omega} f(\boldsymbol{\xi}) G(\mathbf{x}, \boldsymbol{\xi}) d\boldsymbol{\xi} - \int_{\partial\Omega} g(\boldsymbol{\xi}) a(\boldsymbol{\xi}) (\nabla_{\boldsymbol{\xi}} G(\mathbf{x}, \boldsymbol{\xi}) \cdot \mathbf{n}_{\boldsymbol{\xi}}) dS(\boldsymbol{\xi}). \quad \forall \mathbf{x} \in \Omega \quad (3)$$

However, in many cases, it is challenging to find explicit analytical form of the Green’s function (i.e., the solution of Eq. (2)) [39, 37, 38], necessitating its numerical approximation. In this study, we attempt to utilize the GreensONet framework to approximate the unknown Green’s function numerically.

The method for discovering Green’s functions of scalar differential operators can be extended naturally to systems of differential equations. Let  $f = [f^1 \ \dots \ f^{N_f}]^\top : \Omega \rightarrow \mathbb{R}^{N_f}$  be a vector of  $N_f$  forcing terms and  $u = [u^1 \ \dots \ u^{N_u}]^\top : \Omega \rightarrow \mathbb{R}^{N_u}$  be a vector of  $N_u$  system responses such that

$$\mathcal{L} \begin{bmatrix} u^1 \\ \vdots \\ u^{N_u} \end{bmatrix} = \begin{bmatrix} f^1 \\ \vdots \\ f^{N_f} \end{bmatrix}, \quad D \left( \begin{bmatrix} u^1 \\ \vdots \\ u^{N_u} \end{bmatrix}, \Omega \right) = \begin{bmatrix} g^1 \\ \vdots \\ g^{N_u} \end{bmatrix}. \quad (4)$$

We can express the relation between the system’s response and the forcing term using Green’s functions as an integral formulation, i.e.,

$$u^i(x) = \sum_{j=1}^{N_f} \int_{\Omega} G_{i,j}(x, \xi) f^j(\xi) d\xi - \int_{\partial\Omega} g^j(\xi) a^j(\xi) (\nabla_{\xi} G_{i,j}(x, \xi) \cdot \mathbf{n}_{\xi}) dS(\xi), \quad x \in \Omega, \quad (5)$$

for  $1 \leq i \leq N_u$ . Here,  $G_{i,j} : \Omega \times \Omega \rightarrow \mathbb{R} \cup \{\pm\infty\}$  is a component of the Green’s matrix for  $1 \leq i \leq N_u$  and  $1 \leq j \leq N_f$ . Specifically, the  $N_u \times N_f$  matrix of Green’s functions can be written as:

$$G(x, \xi) = \begin{bmatrix} G_{1,1}(x, \xi) & \dots & G_{1,N_f}(x, \xi) \\ \vdots & \ddots & \vdots \\ G_{N_u,1}(x, \xi) & \dots & G_{N_u,N_f}(x, \xi) \end{bmatrix}, \quad x, \xi \in \Omega. \quad (6)$$

Following Eq. (6), we remark that the differential equations decouple, and therefore we can learn each row of the Green’s function matrix independently. That is, for each row  $1 \leq i \leq N_u$ , we train  $N_f$  neural networks to approximate the components  $G_{i,1}, \dots, G_{i,N_f}$ .

Our objective is to construct a neural network, referred to as GreensONet, to approximate the Green’s functions for linear PDE systems. This approach enables the efficient computation of solutions for varying source terms  $f(x)$  and boundary conditions  $g(x)$  by leveraging the approximated Green’s function. To achieve this, the network is trained on a family of source terms  $f(x)$  and boundary conditions  $g(x)$  generated using Gaussian random fields (GRF) [41]. Once trained, the resulting neural network provides a flexible and efficient framework for approximating solutions to the specified PDEs, accommodating previously unseen boundary conditions and source terms while preserving computational efficiency and generalization capability.

### 3. Methodologies

#### 3.1. Framework of GreensONet

The DeepONet architecture is a versatile framework capable of addressing a broad range of problems with varying input parameters. However, its primary limitation lies in the lack of physical interpretability, which results in a high demand for training data to achieve accurate predictions. In this work, we aim to enhance the performance of DeepONet by leveraging the principles of Green’s functions. Specifically, we focus on solving three classical types of PDEs—heat conduction equations, reaction-diffusion equations, and Stokes equations—for both homogeneous and heterogeneous coefficients in 3D bounded domains, as detailed in Section 4.

As shown in Figure 1, the GreensONet framework is designed to efficiently solve complex operator approximation problems by leveraging the principles of Green’s functions, Volterra integral equations and DeepONtes.

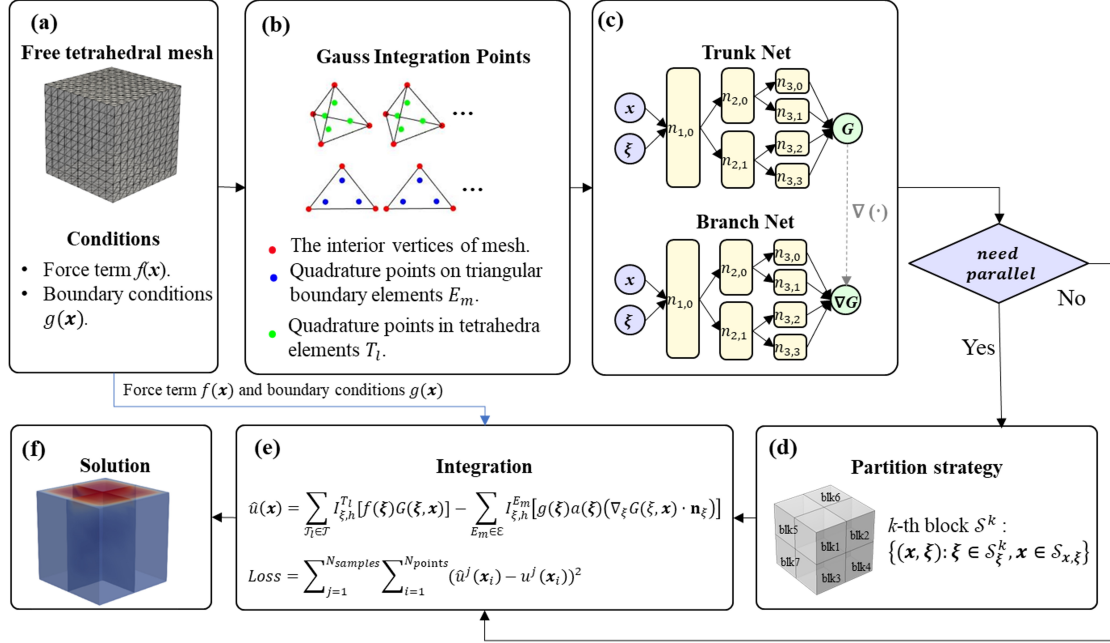


Figure 1: The framework of GreensONet: (a) Import user-defined free tetrahedral mesh and user-defined physical conditions; (b) Calculate the locations of Gauss integration points and integration weights; (c) Constructions of the Trunk Net and Branch Net of the GreensONet based on binary structured neural networks; (d) Domain partition and parallel computation strategy; (e) Volterra integration based on acquired Green's function; (f) The calculated solutions.

The framework begins with the import of a user-defined mesh and physical conditions (step a), followed by the calculation of Gauss integration points and their corresponding weights (step b), which are crucial for accurate numerical integration. In this study, a 4-point Gauss integration rule is applied to all tetrahedral elements within the mesh, while a 3-point Gauss integration rule is used for the triangular boundary faces. Other Gauss integration rules are also available in our code. It is indicated from our experimental results that increasing the number of integration points can improve the accuracy. Our chosen integration scheme strikes a balance between computational efficiency and accuracy.

In step (c), inspired by DeepONet, the Trunk Net and Branch Net are constructed to facilitate the representation of the operator through hierarchical learning. The Trunk Net within GreensONet is designed to approximate the unknown Green's functions  $G(\mathbf{x}, \xi)$  of the system, while the Branch Net are utilized to approximate the auxiliary gradients of the Green's function  $\nabla G(\mathbf{x}, \xi)$ . To achieve this, novel binary-structured neural networks are employed in both the Trunk Net and the Branch Net owing to their strong convergence properties. Furthermore, it is worth noting that for regular domains, the Branch Net can be omitted, as  $\nabla G$  can be efficiently and accurately computed using automatic differentiation. However, for irregular domains, we observe that the accuracy of  $\nabla G$  obtained through automatic differentiation is insufficient. To address this, we employ the Branch Net to learn  $\nabla G$  directly, ensuring greater precision in these cases.

To ensure computational efficiency, step (d) employs domain partitioning based on the principle of independent computation for the Green's function at each point. This approach is further enhanced by parallel computation strategies, enabling the efficient resolution of large-scale problems.

In step (e), Volterra integration is performed using the Green's function obtained in the previous steps, enabling the calculation of the operator's response. By minimizing the deviation between the computed and exact solutions, the Trunk Net and Branch Net are progressively trained until the deviation meets the desired tolerance. Instead of using iterative loops, we directly compute the numerical integration through matrix operations. In contrast, our approach uses multiple global kernels (Green's functions) to perform matrix multiplication with the input features ( $f, g$ ). For

cases with up to 10,000 grid elements, we can compute the global integral in just 0.5 seconds, which is comparable to, or faster than, traditional methods ( $\sim 3$  seconds).

Finally, in step (f), the framework outputs the calculated solutions. This structured approach enhances the scalability and interpretability of GreensONet, making it well-suited for scientific computing and industrial applications. It enables efficient solution approximation for complex PDEs under varying conditions.

The proposed framework is powered by PaddlePaddle [42]. In the following subsections, we will elaborate on each technical detail in turn.

### 3.2. Training datasets

In this subsection, we will elaborate on how to construct a training dataset that incorporates varying boundary conditions and source terms, serving as the foundation for the experiments presented in Section 4. The training dataset consists of  $N$  forcing functions,  $f_j : \Omega \rightarrow \mathbb{R}$  and boundary conditions,  $g_j : \partial\Omega \rightarrow \mathbb{R}$ , and associated system responses,  $u_j : \Omega \rightarrow \mathbb{R}$ , which are solutions to the following equation:

$$\mathcal{L}u_j = f_j, \quad \mathcal{D}(u_j, \Omega) = g_j, \quad (7)$$

where  $\mathcal{L}$  is a linear differential operator,  $\mathcal{D}$  is a linear operator acting on the boundary.  $f_j$  is the source term and  $g_j$  is the constraint on the boundary. The training data comprises  $N$  data pairs, where the forcing terms or the boundary conditions are drawn at random from a Gaussian process,  $\mathcal{GP}(0, \mathcal{K})$ , and  $\mathcal{K}$  is the squared-exponential covariance kernel [41] defined as

$$\mathcal{K}(\mathbf{x}_i, \mathbf{x}_j) = \exp\left(-\frac{1}{2} \sum_{d=1}^3 \left(\frac{x_{id} - x_{jd}}{\ell_d}\right)^2\right). \quad (8)$$

where  $\mathbf{x}_i = (x_{i1}, x_{i2}, x_{i3})$  and  $\mathbf{x}_j = (x_{j1}, x_{j2}, x_{j3})$  are two points in three-dimensional space.  $\ell_d$  denotes the length-scale parameter for each dimension  $d$ . The parameter  $\ell_d > 0$  governs the correlation between the values of  $f \sim \mathcal{GP}(0, \mathcal{K})$  at points  $\mathbf{x}_i$  and  $\mathbf{x}_j$ , where  $\mathbf{x}_i, \mathbf{x}_j \in \Omega$ . As shown in Figure 2, a smaller value of  $\ell_d$  results in more oscillatory random functions. The diversity of the training set caused by  $\ell_d$  is essential for capturing the different modes of the operator  $\mathcal{L}$  and accurately learning the corresponding Green's function, as discussed in [43]. In this work,  $\ell_d$  is selected within the range  $[0.1, 1]$ , depending on the specific problem under consideration.

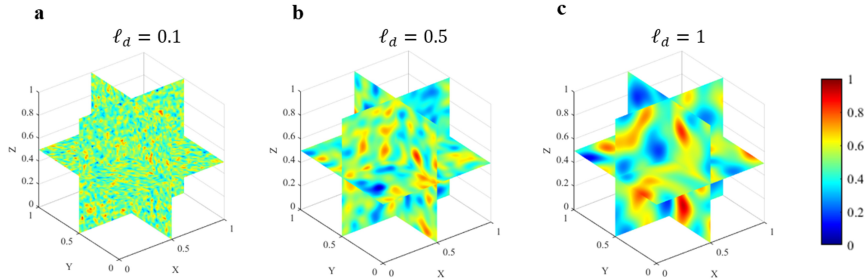


Figure 2: 3D Gaussian Field with different  $\ell_d$ : **a.** 3 slices-Gaussian Field when  $\ell_d = 0.1$ ; **b.** 3 slices-Gaussian Field when  $\ell_d = 0.5$ ; **c.** 3 slices-Gaussian Field when  $\ell_d = 1$ .

### 3.3. Numerical quadrature and Loss function

The computation of Eq. (3) is central to this method, where Gaussian quadrature is employed to approximate it. Specifically, the computational domain  $\Omega$  is discretized into a mesh composed of unstructured tetrahedral elements in the interior and triangular surfaces on the boundaries. Specifically, the interior domain is divided into tetrahedral elements denoted as  $\mathcal{T} = \{T_l\}$ , while the boundary is represented by triangular faces denoted as  $\mathcal{E}^{\text{bdry}} = \{E_m\}$ .

For the tetrahedral elements  $T_l$ , a 4-point Gaussian quadrature is employed. For the triangular faces  $E_m$ , a 3-point Gaussian quadrature is utilized. The formulas for determining the Gaussian quadrature points and their corresponding weights are provided as follows:

$$\begin{aligned}
\text{3-point quadrature rule on } E_m : \quad \eta = [\eta_{i1}, \eta_{i2}, \eta_{i3}] &= \begin{bmatrix} \frac{2}{3} & \frac{1}{6} & \frac{1}{6} \\ \frac{1}{6} & \frac{2}{3} & \frac{1}{6} \\ \frac{1}{6} & \frac{1}{6} & \frac{2}{3} \end{bmatrix}, \quad \mathbf{w} = \begin{bmatrix} \frac{1}{3} \\ \frac{1}{3} \\ \frac{1}{3} \end{bmatrix}. \\
\text{4-point quadrature rule on } T_l : \quad \zeta = [\zeta_{i1}, \zeta_{i2}, \zeta_{i3}] &= \begin{bmatrix} 0.58541020 & 0.13819660 & 0.13819660 \\ 0.13819660 & 0.58541020 & 0.13819660 \\ 0.13819660 & 0.13819660 & 0.58541020 \\ 0.13819660 & 0.13819660 & 0.13819660 \end{bmatrix}, \quad \mathbf{w} = \begin{bmatrix} \frac{1}{4} \\ \frac{1}{4} \\ \frac{1}{4} \\ \frac{1}{4} \end{bmatrix}.
\end{aligned}$$

Here, each row of the matrix  $\eta$  and  $\zeta$ , denoted as  $\eta_i = [\eta_{i1}, \eta_{i2}, \eta_{i3}]$  and  $\zeta_i = [\zeta_{i1}, \zeta_{i2}, \zeta_{i3}]$ , represents the coordinates of the  $i$ -th Gaussian point.

Then Eq. (3) can be approximated as:

$$\hat{u}(\mathbf{x}) \approx \sum_{T_l \in \mathcal{T}} I_{\xi, h}^{T_l} [f(\xi)G(\xi, \mathbf{x})] - \sum_{E_m \in \mathcal{E}^{\text{bdry}}} I_{\xi, h}^{E_m} [g(\xi)a(\xi)(\nabla_{\xi}G(\xi, \mathbf{x}) \cdot \mathbf{n}_{\xi})]. \quad (9)$$

Here  $I_{\xi, h}^{T_l}[\cdot]$  denotes the numerical quadrature for evaluating  $\int_{T_l} f(\xi)G(\xi, \mathbf{x})d\xi$  and  $I_{\xi, h}^{E_m}[\cdot]$  the quadrature for evaluating  $\int_{E_m} g(\xi)a(\xi)(\nabla_{\xi}G(\xi, \mathbf{x}) \cdot \mathbf{n}_{\xi})dS(\xi)$ , respectively. In Eq. (9),  $\xi$  in  $I_{\xi, h}^{T_l}[\cdot]$  represents the Gaussian quadrature points from all elements in the mesh, with a total length of  $N_{\text{elements}} \times 4$ . Similarly,  $\xi$  in  $I_{\xi, h}^{E_m}[\cdot]$  corresponds to the Gaussian quadrature points from all boundary elements of the mesh, with a total length of  $N_{\text{boundary\_elements}} \times 3$ . As illustrated in Fig. 3, the computational complexity for evaluating the numerical quadrature at a single point  $\mathbf{x}$  is  $O(N_{\text{elements}} + N_{\text{boundary\_elements}})$ . For all points in the geometric domain, the overall complexity is  $O(N_{\text{points}} \times (N_{\text{elements}} + N_{\text{boundary\_elements}}))$ .

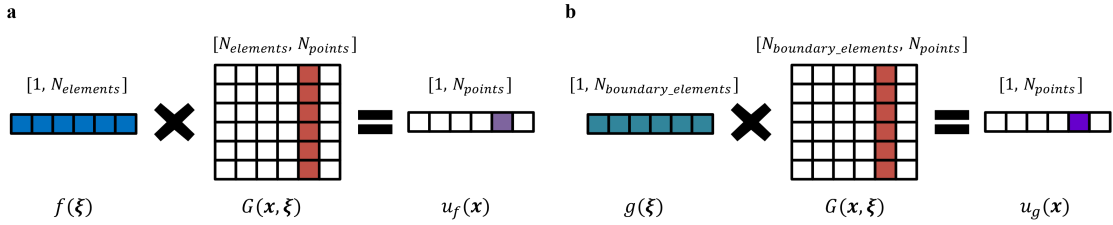


Figure 3: Illustration of numerical quadrature: (a)  $I_{\xi, h}^{T_l} [f(\xi)G(\xi, \mathbf{x})]$  over the domain; (b)  $I_{\xi, h}^{E_m} [g(\xi)\nabla_{\xi}G(\xi, \mathbf{x})]$  over the boundary.

In our experiments, the loss function is defined as Eq. (10). For a case involving 10,000 grid elements, the quadrature computation time is approximately 0.5 seconds, and the total training time is about 1 hour with 1.5 seconds for per training epoch. In prior studies [37, 38], Green's functions were approximated within a data-free framework. The loss function was formulated as  $Loss = (\mathcal{L}G(\mathbf{x}, \xi) - \rho(\mathbf{x}, \xi))^2$ , where  $\rho(\mathbf{x}, \xi)$  denotes a Gaussian density function used to approximate the Dirac delta function. Although this approach eliminates the need for training data, its scalability is hindered by the computational cost of automatic differentiation, resulting in training times of up to 13 hours for 2D problems. In contrast, the proposed method substantially enhances training efficiency and accelerates convergence, enabling practical applications to more computationally demanding 3D problems. Furthermore, the discrepancy between the Gaussian density function  $\rho(\mathbf{x}, \xi)$  and the exact Dirac delta function  $\delta(\mathbf{x} - \xi)$  is compounded through the superposition principle during the integration process for obtaining the solution. This cumulative amplification of the error ultimately degrades the accuracy of the final solution. The enhanced efficiency and accuracy are key advantages of our approach.

$$Loss = \sum_{j=1}^{N_{\text{samples}}} \sum_{i=1}^{N_{\text{points}}} (\hat{u}^j(\mathbf{x}_i) - u^j(\mathbf{x}_i))^2, \quad \mathbf{x}_i \in \Omega, \quad i = 1, \dots, N_{\text{points}}, \quad j = 1, \dots, N_{\text{samples}}. \quad (10)$$



### 3.4. Binary structured neural network

In this paper, we employ the binary structured neural network (BsNN) [44] as the fundamental component of both the Trunk Net and the Branch Net. The BsNN is designed with the inspiration of ‘‘mixture of experts’’ (MoEs) model [45], where the model comprises multiple independent expert networks. Each expert network specializes in solving a subproblem within a complex task, and their collective knowledge is combined to address the overall complex problem. The BsNN is similar to MoE, composed of multiple sub-networks, with each sub-network dedicated to learning a specific local feature of the solution and the collective knowledge gained by these sub-networks represents the complete set of solution features.

Compared with feed-forward neural networks (FNN), BsNN demonstrate superior efficiency and effectiveness in capturing the local features of solutions [44]. The rationale for selecting BsNN lies in the observation that the Green’s functions possess singularities near the diagonal [43]. In experiments demonstrated in Section 4.1, it is again validated that BsNN achieve faster convergence compared to FNN. Moreover, for cases where FNN fail to converge (see Section 4.2 (b)), BsNN successfully achieve normal convergence, further highlighting their robustness and efficiency.

The general network structure of BsNNs is illustrated in Figure 4 a. Each  $n_{i,j}$  in Figure 4 a contains one or more neurons, and such  $n_{i,j}$  is referred to as a ‘‘neuron block’’. The black arrows indicate fully connected relationship between two neuron blocks, reflecting trainable weight parameters connecting every neuron pair from the two neural blocks. Within the final layer, the outputs of each neuron block are concatenated and fully connected to the output. This structure resembles a binary tree, where the neuron blocks in each hidden layer, except the first and the last, are fully connected to two neuron blocks in the next hidden layer. When the network possesses substantial depth, the parameter count of a BsNN is notably lower than that of an equivalently sized FNN featuring the same quantity of neurons. In the experiments conducted in this study, the number of parameters in the BsNN is approximately 1093, compared to 1393 in the FNN, representing a reduction of approximately 21%.

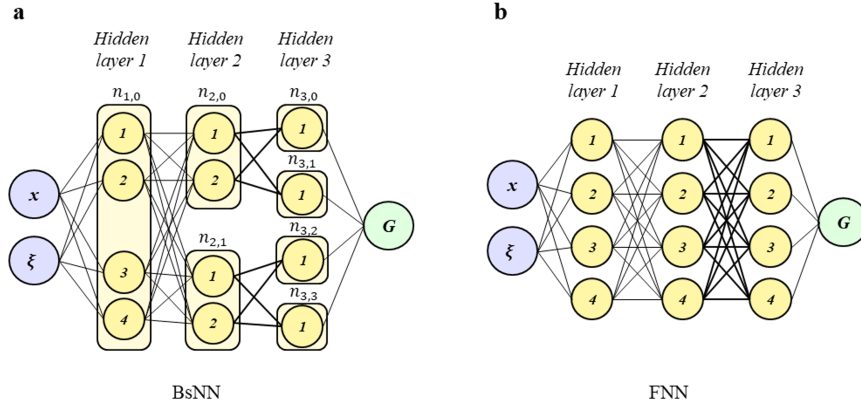


Figure 4: **a.** The structure of a BsNN consists of 3 hidden layers, each with 4 neurons (except the first and the last hidden layers, the neuron blocks in each hidden layer are fully connected to two neuron blocks in the next hidden layer). **b.** The structure of a FNN consists of 3 hidden layers, each with 4 neurons.

In BsNN,  $w_{i,j}$ ,  $b_{i,j}$ , and  $\zeta_{i,j}$  represent the weight, bias, and activation function, respectively, for the  $j$ -th branch of the  $i$ -th hidden layer ( $j = 0, 1, \dots, 2^i - 1, i = 0, 1, \dots, n - 2$ ). Correspondingly,  $w_{n-1}$ ,  $b_{n-1}$ , and  $\zeta_{n-1}$  denote the weight, bias, and activation function for the final layer. Each neuron block within the same hidden layer contains the same number of neurons, and this quantity is known as the ‘‘block size’’ of that hidden layer. In this paper, the number of neuron blocks for the  $i$ -th layer with  $1 \leq i < n$  is  $2^{i-1}$ , and for  $1 < i < n$ , the block size in the  $(i - 1)$ -th layer is twice that of the  $i$ -th layer. With these notations, the forward propagation of the BsNN can be mathematically expressed as follows:

$$o_{i,j} = \zeta_{i-1,j} \left( w_{i-1,j} o_{i-1, \lfloor \frac{j}{2} \rfloor} + b_{i-1,j} \right), \quad i = 1, \dots, (n - 1), j = 0, \dots, (2^{i-2} - 1). \quad (11)$$

The outputs  $o_{n-1,j}$  (where  $j = 0, 1, \dots, 2^{n-2} - 1$ ) are concatenated along the last dimension to create a variable

referred to as  $o_{n-1}$ . Subsequently, the final output of the BsNN is obtained as follows

$$o_n = \varsigma_{n-1} (w_{n-1}o_{n-1} + b_{n-1}). \quad (12)$$

### 3.5. Parallel strategy for efficient calculation

When handling a large dataset  $\mathbf{x} \subset \Omega$ , computing Eq. (9) and performing backpropagation during training on a single GPU becomes computationally prohibitive. Since the Green's function corresponding to each point  $\mathbf{x} \in \Omega$  can be computed independently, the domain  $\Omega$ , or equivalently the set of points  $\mathbf{x}$ , can be partitioned to facilitate parallel computation. As illustrated in Fig. 5, two partitioning strategies can be employed: (a) dividing the computational domain  $\Omega$  into several subdomains of approximately equal size, with each subdomain consisting of a subset of points; or (b) directly splitting the entire set of points into several subsets of comparable size. For the computation of GreensONets, both strategies are largely equivalent in terms of parallelization efficiency. By assigning each partition to an independent GPU for parallel computation, the overall computational efficiency can be significantly improved.

We propose a highly parallelizable strategy for processing  $\mathbf{x}$ . Specifically, we partition the point set  $\mathcal{S} = \{(\mathbf{x}, \boldsymbol{\xi}) : \mathbf{x}, \boldsymbol{\xi} \in \Omega\}$  into  $K$  subsets of approximately equal size, denoted by  $\mathcal{S}^k = \{(\mathbf{x}, \boldsymbol{\xi}) : \mathbf{x} \in \mathcal{S}_x^k, \boldsymbol{\xi} \in \mathcal{S}_{x,\boldsymbol{\xi}}\}$ , where  $k = 1, \dots, K$ , and  $n_{\text{points}}$  is the total number of points in  $\mathcal{S}$ . For each subset, a sub-training process is conducted to train the GreensONet, gradually fine-tuning their parameters for each  $\mathbf{x}$ -block until all blocks have been processed. Using these partitioned samples, the complete training process is composed of  $K$  sub-training tasks, each utilizing the data points in  $\mathcal{S}_x^k$ . This approach naturally decomposes the training workload into smaller, independent subtasks, enabling efficient parallelization and implementation across multiple GPUs.

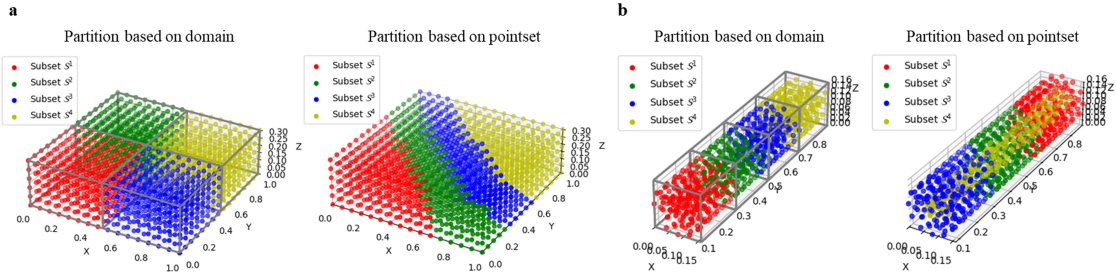


Figure 5: Illustration of point set partition strategy: **a** partition strategy based on the domain of the regular plat, partition strategy based on the point-set of the regular plat; **b** partition strategy based on the domain of the pipe, partition strategy based on the point-set of the pipe.

### 3.6. Similarities and differences with DeepONet

To better illustrate the similarities and differences between our method and DeepONet, we depict their respective structures in Fig. 6. DeepONet consists of two Branch Nets and one Trunk Net. The Trunk Net takes coordinate information as input, while the two Branch Nets encode the source term and boundary conditions, respectively. The outputs of the Trunk Net and the Branch Nets are combined using the Hadamard product, followed by a summation to yield the target physical quantity. It is worth noting that for multi-dimensional target quantities, the summation step is omitted.

In contrast, GreensONet requires only one Trunk Net and one Branch Net. Both the Trunk Net and the Branch Net take coordinate information as input, with their outputs representing the desired Green's function and its gradient. Notably, the gradient of the Green's function can alternatively be computed via automatic differentiation, in which case the Branch Net can be omitted. The target physical quantity is then obtained through numerical integration of the outputs. For multi-dimensional physical quantities, Green's function matrices are learned by employing multiple pairs of Trunk Nets and Branch Nets. These matrices are subsequently integrated with the boundary conditions and source terms to compute the desired quantities. In summary, while DeepONet relies on multiple Branch Nets and a Trunk Net with Hadamard product operations to approximate target quantities, GreensONet adopts a more streamlined approach by leveraging numerical integration of Green's functions, offering greater flexibility and efficiency.

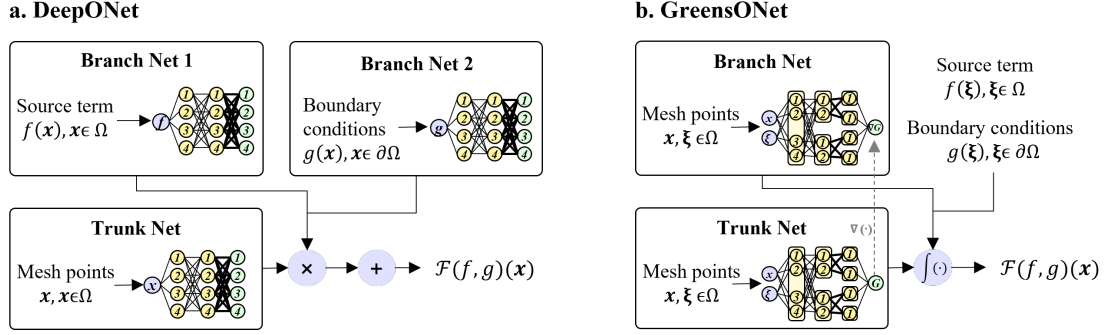


Figure 6: Illustration of (a) structure of DeepONet and (b) structure of GreensONet.

The algorithm of the GreensONet can be summarized as follow:

---

**Algorithm 1** Solving PDEs by GreensONet and acquiring Green's function

---

- 1: **Input:**  $\mathcal{L}(\cdot)$ ,  $f(\mathbf{x})$  and  $g(\mathbf{x})$ , the mesh  $\mathcal{T}_q$ , and an interior vertex  $\mathbf{x} \in \Omega$
  - 2: **Output:** The PDE solution at  $\mathbf{x} : u(\mathbf{x})$
  - 3: Generate the quadrature points and quadrature weights for each element.
  - 4: Calculate the normal and volume for each element in the domain.
  - 5: Calculate the area for each element on the boundary.
  - 6: **if** need parallel **then**
  - 7:   Apply the domain partition to divide  $S_{\mathbf{x}, \xi}$  into  $K$  blocks ( $K > 1$ ).
  - 8: **else**
  - 9:    $K=1$ .
  - 10: **end if**
  - 11: **for**  $1, N_{samples}$  **do**
  - 12:   **for**  $k=1, \dots, K$  **do**
  - 13:     **for**  $1, \dots, N_{epoches}$  **do**
  - 14:       Feed all points in  $S_{\mathbf{x}, \xi}^k$  into the Branch Net and Trunk Net.
  - 15:       Acquire  $G(\mathbf{x}, \xi; \Theta)$  and  $\nabla G(\mathbf{x}, \xi; \Theta)$ .
  - 16:       Calculate  $\hat{u}(\mathbf{x})$  by integration defined in Eq. (9).
  - 17:       Calculate error of  $(\hat{u}(\mathbf{x}) - u(\mathbf{x}))^2$ .
  - 18:       Optimize parameters  $\Theta$  of the Branch Nets and Trunk Nets to minimize error of  $(\hat{u}(\mathbf{x}) - u(\mathbf{x}))^2$ .
  - 19:     **end for**
  - 20:   **end for**
  - 21: **end for**
  - 22: Return well-trained Greens' function.
- 

#### 4. Experiments and results

In this section, we evaluate the performance of the proposed GreensONet framework for approximating Green's functions and its application to efficiently solving three classical PDEs using Algorithm 1. The investigated cases include:

1. *Steady Heat Conduction Equation*: This case examines scenarios involving a finned tube under varying boundary conditions.
2. *Heterogeneous Reaction-Diffusion Equations*: Two scenarios are considered: homogeneous diffusion on a flat plate and heterogeneous mixing between two substances within a micro-pipe.

3. *Stokes Equations*: The analysis focuses on the effects of source terms on fluid flow. In contrast to the previous cases, this investigation involves constructing a Green’s function matrix to solve for multidimensional velocity variables.

For each case, we detail the specific hyperparameters used for GreensONet and the baseline models in the corresponding subsections. All neural networks are implemented with ReLU activation functions, and training is conducted using the Adam optimizer. The  $L_2$  norm is adopted to quantify approximation errors. All experiments reported in this study were performed on a remote server running Ubuntu 22.04 LTS, equipped with an Intel® Xeon® Platinum 8380 CPU @ 2.30GHz and an NVIDIA A100 GPU with 80GB of HBM2 memory.

#### 4.1. Case 1: Steady heat conduction equations

Heat conduction equations play a fundamental role in mathematical physics and engineering, governing a wide range of phenomena such as metal smelting and heat dissipation in electronic components. In this study, we focus on the efficient solutions of the steady heat conduction equations under varying boundary conditions (ref. eq 13), which is critical for capturing diverse physical scenarios. A classical heat transfer case on the finned tube is considered. The physical condition setting and results are demonstrated below.

$$\begin{cases} \nabla^2 u(\mathbf{x}) = Q(\mathbf{x}), & \mathbf{x} \in \Omega \\ u(\mathbf{x}) = g(\mathbf{x}). & \mathbf{x} \in \partial\Omega \end{cases} \quad (13)$$

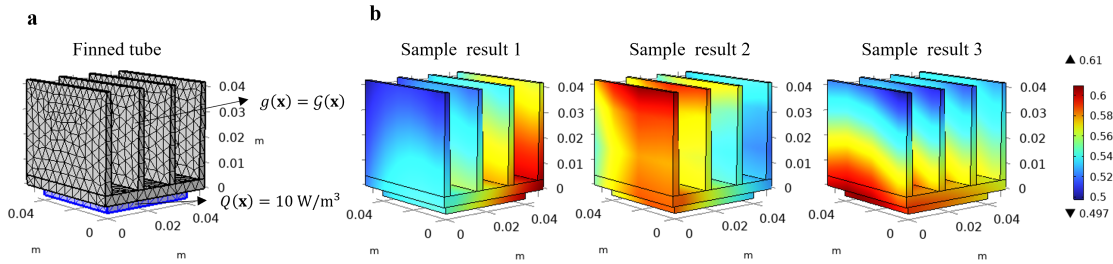


Figure 7: (a) The simulation setting of the steady heat conduction case on finned tube; (b) sample results with generated GRF conditions.

As illustrated in Figure 7, the source term  $Q(\mathbf{x})$  is set to 10 on the heated bottom plate, while the Dirichlet boundary condition  $g(\mathbf{x})$  is derived from a GRF with a wavelength parameter  $\lambda = 1$ . For the finned tube geometry, the computational mesh consists of 4427 tetrahedral cells and 1478 vertices within the domain, along with 2968 triangular faces on the boundary. The GRF boundary condition is applied to the top surface. In this study, we generated 100 datasets, with sample results illustrated in Figure 7 b. Among these, 80 datasets were used for training and 20 for testing.

For validation, we compared the GreensONet framework against four well-known models: PINN [16], DeepONet [6], PI-DeepONet [8], and FNO [18]. A detailed introduction to PINN, DeepONet, PI-DeepONet, and FNO can be found in Section 1. Table 1 and Figure 8 present a comprehensive comparison between GreensONet and these baseline models on the finned tube. To ensure a fair evaluation, we used identical hyperparameters across all models, including learning rate and optimizer settings. Additionally, given the variations in convergence rates among the different networks, we selected a sufficient number of iterations for each model to ensure convergence. To better assess the performance of each network, we kept the number of layers as consistent as possible across all models.

As shown in Table 1, for irregular geometries, GreensONet achieves the lowest testing error compared to PINN, DeepONet, PI-DeepONet, and FNO. It is important to note that FNO can only handle cases with regular geometries, requiring the finned tube geometry to be interpolated onto a structured grid for input into the FNO, with the output subsequently interpolated back to the original geometry. While this process introduces interpolation errors, these are systematic errors that affect both the training and testing datasets equally. However, FNO exhibits significant overfitting, as highlighted in Table 1. It achieves the lowest training error ( $\text{MSE} = 1.28 \times 10^{-5}$ ) but suffers a substantial increase in testing error ( $\text{MSE} = 6.31 \times 10^{-4}$ ). Figure 8 further illustrates this limitation: although FNO captures

the overall trend of the temperature distribution, it fails to represent fine-scale details accurately, especially when compared to GreensONet. In contrast, GreensONet demonstrates superior generalization. While its training error ( $\text{MSE} = 4.59 \times 10^{-5}$ ) is higher than that of FNO, it achieves the lowest testing error ( $\text{MSE} = 1.26 \times 10^{-5}$ ). This underscores the importance of incorporating physics-informed priors to enhance the generalization capabilities of neural networks.

As summarized in Table 1, GreensONet achieves the lowest testing error among all evaluated models, including PINN, DeepONet, PI-DeepONet, and FNO, for cases involving irregular geometries. It is noteworthy that FNO is inherently limited to regular geometries and requires interpolation to map the finned tube geometry onto a structured grid for input, with subsequent interpolation of the output back to the original geometry. As indicated in Table 1, FNO demonstrates significant overfitting. Despite achieving the lowest training error ( $\text{MSE} = 1.28 \times 10^{-5}$ ), its testing error increases substantially ( $\text{MSE} = 6.31 \times 10^{-4}$ ). This limitation is further evident in Figure 8, where FNO captures the general trend of the temperature distribution but fails to accurately represent fine-scale details, particularly when compared to GreensONet. In contrast, GreensONet exhibits robust generalization capabilities. Although its training error ( $\text{MSE} = 4.59 \times 10^{-5}$ ) is higher than that of FNO, it achieves the lowest testing error ( $\text{MSE} = 1.26 \times 10^{-5}$ ). This highlights the effectiveness of incorporating physics-informed priors in enhancing the generalization performance of neural networks.

In this case, DeepONet consists of a Trunk Net with layers [3, 12, 12, 12, 4] to process position information  $\mathbf{x}$ , along with two Branch Net: Branch Network 1 for handling the force term  $Q$  and Branch Network 2 for managing boundary conditions  $g$ , as detailed in Table 1. In this setup,  $N_{\text{points}}$  denotes the total number of points in the domain, which is 1478 for the finned tube. As shown in Table 1, DeepONet achieves an  $L_2$  error of  $8.02 \times 10^{-4}$  on the test set. PI-DeepONet, which incorporates the same Trunk Net and additional Branch Net (Branch Net 1 and Branch Net 2), results in a lower  $L_2$  error of  $5.04 \times 10^{-4}$  compared to DeepONet. Furthermore, as shown in the 2<sup>nd</sup> row and 2<sup>nd</sup> column of Figure 8, the distribution of isotherms in PI-DeepONet better aligns with the exact solution than that of DeepONet (2<sup>nd</sup> row, 1<sup>st</sup> column of Figure 8). This improvement may be attributed to the incorporation of the PDE constraints in the loss function.

PINN, which uses a similar five-layer structure [3, 12, 12, 12, 1] as GreensONet, achieved an  $L_2$  error of  $2.29 \times 10^{-2}$  after 10000 epochs. Boundary and PDE constraints were incorporated into the loss function as soft penalties. The PDE loss is approximately  $1.46 \times 10^{-1}$  and could not decrease further. This suggests that, for the random GRF boundary conditions, PINN may not be able to simultaneously satisfy both the random boundary condition and the PDE constraints using the Adam optimization algorithm.

Across all visualizations, GreensONet is the only model capable of accurately capturing the full range of the temperature field, as indicated by the colorbar. Other baseline models exhibit varying degrees of deviation in this regard. Furthermore, as shown in the isotherm distribution plots in Figure 9, the temperature isotherms predicted by GreensONet closely align with the actual distributions. In contrast, while FNO captures the general trend, it introduces noticeable disturbances in regions where the actual isotherms are smooth, further highlighting the advantage of GreensONet in handling irregular geometries effectively.

In this study, we further investigated the impact of BsNN and FNN architectures on the performance of the GreenONet framework. Under the BsNN architecture, the GreenONet framework achieved a training error of  $4.59 \times 10^{-5}$  within only 2000 epochs. In contrast, using the FNN architecture with the same network depth, the framework required 6000 epochs to reach a training error of  $6.37 \times 10^{-5}$ . These results underscore the advantages of adopting the GreenONet framework for efficient and accurate operator approximation.

This case demonstrates the boundary condition adaptability of our method, highlighting its robustness and versatility in solving the heat conduction equation on both regular and irregular computational domains with varying boundary conditions.

Table 1: The hyper-parameters and performance of different baseline models on case of finned tube.

Model	Epochs	Learning rate	Layers	Training error	Testing error
GreensONet	2000	0.001	[6, 12, 12, 12, 1]	$4.59 \times 10^{-5}$	$1.26 \times 10^{-5}$
PINN	10000	0.001	[3, 12, 12, 12, 1]	-	$2.29 \times 10^{-2}$
DeepONet	2000	0.001	Trunk Net: [3, 12, 12, 12, 4] Branch Net 1: [ $N_{points}$ , 12, 12, 12, 4] Branch Net 2: [ $N_{points}$ , 12, 12, 12, 4]	$8.02 \times 10^{-4}$	$1.81 \times 10^{-3}$
PI-DeepONet	2000	0.001	Trunk Net: [3, 12, 12, 12, 4] Branch Net 1: [ $N_{points}$ , 12, 12, 12, 4] Branch Net 2: [ $N_{points}$ , 12, 12, 12, 4]	$5.04 \times 10^{-4}$	$1.62 \times 10^{-3}$
FNO	2000	0.001	[6, 12, 12, 12, 12, 1]	$1.28 \times 10^{-5}$	$6.31 \times 10^{-4}$

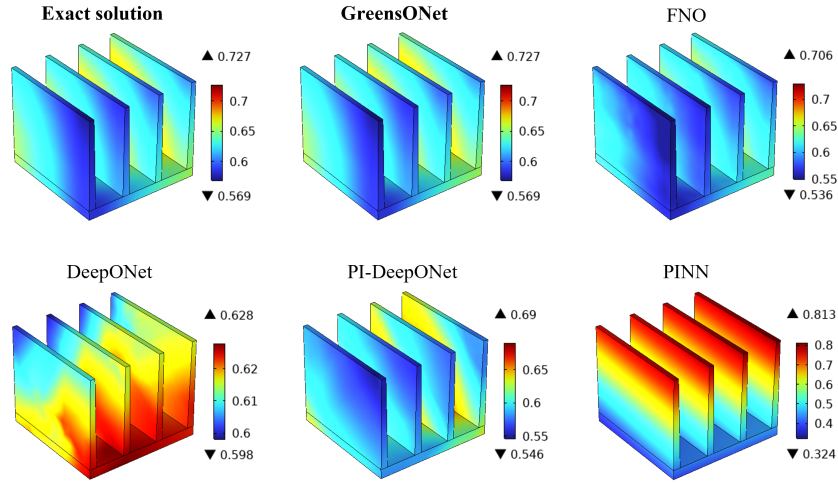


Figure 8: Case study for steady heat conduction equation: temperature distribution from exact solution, and inference of GreensONet, FNO, DeepONet, PI-DeepONet, PINN (from left column to right column, from first row to second row).

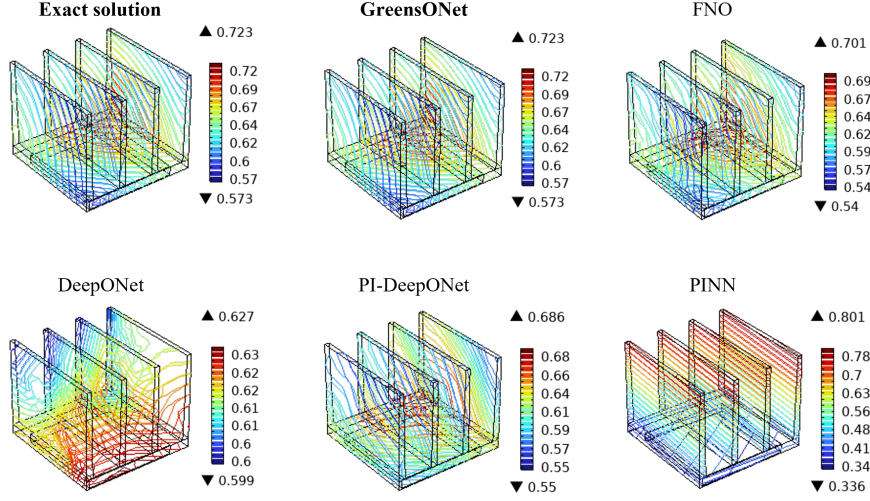


Figure 9: Case study for steady heat conduction equation on finned tube: isotherm distribution from exact solution, GreensONet, FNO, DeepONet, PI-DeepONet, PINN (from left column to right column, from first row to second row).

#### 4.2. Case 2: Heterogeneous reaction-diffusion equations

Reaction-diffusion equations play a crucial role in modeling complex spatial and temporal patterns in biological, chemical, and physical systems. They are particularly significant in studying phenomena such as pattern formation in developmental biology, the spread of diseases, and ecological dynamics. Additionally, they are widely applied in materials science for the study of diffusion processes and phase transitions. In this work, we focus on steady heterogeneous reaction-diffusion equations under varying source terms. The study explores two classical cases: one in (a) a flat plate geometry and the other (b) in a pipe configuration. These models serve as representative examples to investigate the impact of spatially varying sources on the reaction-diffusion dynamics in different domains, with heterogeneous diffusion coefficients. The physical condition setting and results are demonstrated below.

$$\begin{cases} -\nabla \cdot (a(\mathbf{x})\nabla u(\mathbf{x})) + r(\mathbf{x})u(\mathbf{x}) = f(\mathbf{x}), & \mathbf{x} \in \Omega \\ u(\mathbf{x}) = g(\mathbf{x}). & \mathbf{x} \in \partial\Omega \end{cases} \quad (14)$$

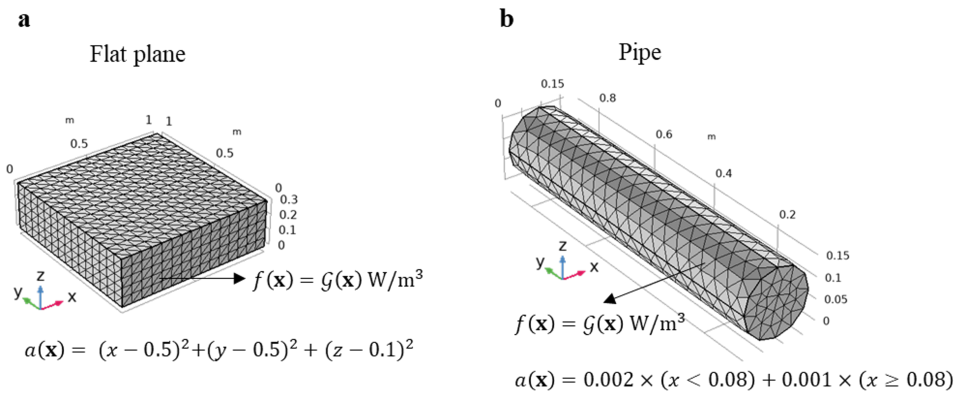


Figure 10: **a.** The simulation setting of the steady heterogeneous reaction-diffusion case on flat plane. **b.** The simulation setting of the steady heterogeneous reaction-diffusion case on pipe.

**(a) Reaction-diffusion equations case on a flat plate.** As shown in Figure 10 (a), in this case, the diffusion coefficient is set as  $a(\mathbf{x}) = (x - 0.5)^2 + (y - 0.5)^2 + (z - 0.1)^2$ , and the force term  $f(\mathbf{x})$  is generated by the GRF with a

wavelength parameter  $\lambda = 1$ . This setup is designed to simulate a natural phenomenon where diffusion is faster at the edges and slower in the center. For the flat plane, the mesh consists of 6750 equally sized tetrahedral cells and 1536 vertices within the domain, along with 1500 equally sized triangular faces on the boundary. In this study, we generated 100 datasets, of which 80 datasets were used for training and 20 datasets for testing. In this case, we also consider comparisons with four baseline models (FNO, DeepONet, PI-DeepONet, and PINN). The network hyperparameters and the comparison of results are shown in Table 2 and Figure 11. The error in Table 2 was quantified by mean square error (MSE).

From Table 2 and Figure 11, we observe that FNO achieves better performance on the training set (MSE =  $4.96 \times 10^{-5}$ ) compared to GreensONet (MSE =  $4.06 \times 10^{-4}$ ). However, FNO exhibits significant overfitting on the validation set, with an MSE of  $1.09 \times 10^{-3}$ , while GreensONet demonstrates good generalization, with the validation error of  $3.06 \times 10^{-4}$ . This further supports our observations that, for purely data-driven algorithms, the generalization capability will be weakened as the complexity of the problem increases.

Consistent with the observations in Section 4.1, Figure 11 shows that DeepONet and PI-DeepONet perform worse than FNO and GreensONet, with testing MSE errors of  $3.12 \times 10^{-3}$  and  $3.63 \times 10^{-3}$ , respectively. Furthermore, PINN encounters convergence difficulties, resulting in a significantly higher MSE error of  $7.68 \times 10^{-2}$ . These results validate the limitations of MLP-based methods compared to CNN-based frameworks, such as FNO, in effectively learning from high-dimensional data, as stated in [6]. Notably, although GreensONet is also based on an MLP architecture, it surpasses the performance of FNO, underscoring the importance of incorporating physics-informed priors to enhance model effectiveness.

It is important to highlight that, although the design of GreenONet involves integration, this operation has been efficiently converted into matrix computations, significantly reducing both inference and training times. In this case, the computational time for the finite element method is approximately 3 seconds. In comparison, GreenONet achieves an inference time of 0.4 seconds, with a total training time of 23 minutes (1.4 seconds per epoch). For DeepONet, the inference time is 0.57 seconds, and the training time is 19 minutes. The FNO demonstrates an inference time of 0.22 seconds and a training time of 3 minutes, while the PINN requires 67.5 minutes for training. The computational speeds of GreensONet is comparable to other deep learning methods and outperforms the traditional FEM. Furthermore, GreenONet inherently benefits from the superposition principle of Green’s function computation, making it naturally parallelizable. For larger-scale mesh problems, the block algorithm introduced in Section 3 can be applied to further accelerate both the training and inference processes of GreenONet.

Table 2: The hyper-parameters and performance of different baseline models on case of flat plane.

Model	Epochs	Learning rate	Layers	Training error	Testing error
GreensONet	1000	0.001	[6, 12, 12, 12, 1]	$4.06 \times 10^{-4}$	$3.06 \times 10^{-4}$
PINN	15000	0.001	[3, 12, 12, 12, 1]	-	$7.68 \times 10^{-2}$
DeepONet	2000	0.001	Trunk Net: [3, 12, 12, 12, 1] Branch Net 1: [ $N_{points}$ , 12, 12, 12, 1] Branch Net 2: [ $N_{points}$ , 12, 12, 12, 1]	$3.91 \times 10^{-2}$	$3.12 \times 10^{-2}$
PI-DeepONet	1000	0.001	Trunk Net: [3, 12, 12, 12, 1] Branch Net 1: [ $N_{points}$ , 12, 12, 12, 1] Branch Net 2: [ $N_{points}$ , 12, 12, 12, 1]	$3.93 \times 10^{-2}$	$3.63 \times 10^{-2}$
FNO	2000	0.001	[6, 6, 6, 6, 6, 1]	$4.96 \times 10^{-5}$	$1.09 \times 10^{-3}$



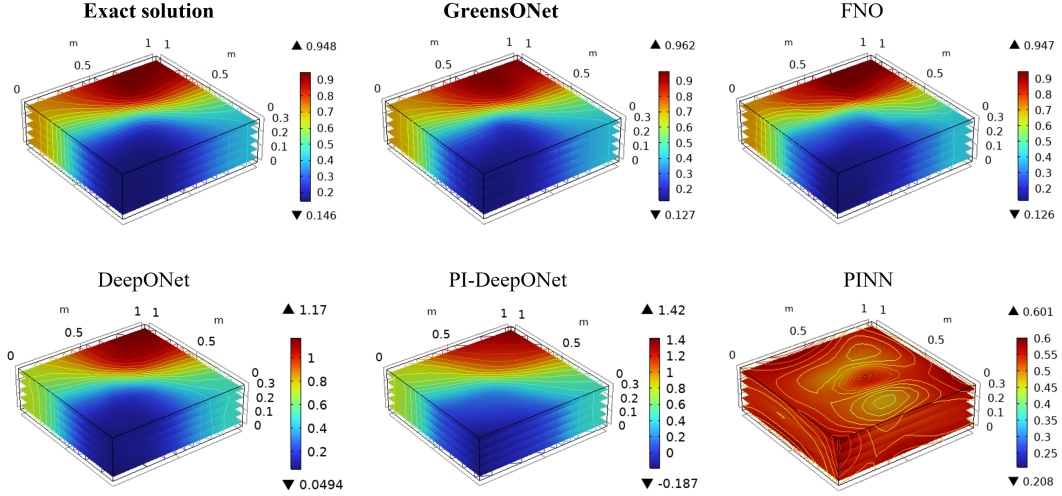


Figure 11: Case study for steady heterogeneous reaction-diffusion on flat plane: physical distribution and isotherm distribution from exact solution, and inference of GreensONet, FNO, DeepONet, PI-DeepONet, PINN (from left column to right column, from first row to second row).

**(b) Reaction-diffusion equations case on a pipe.** As shown in Figure 10, in this case, the diffusion coefficient is set as a heaviside function  $a(\mathbf{x}) = 0.002(x < 0.08) + 0.001(x \geq 0.08)$ , and the force term  $f(\mathbf{x})$  is generated by the GRF with a wavelength parameter  $\lambda = 1$ . Here, we set the diffusion coefficient as a step function to simulate a common mixing phenomenon between two substances in a micro pipe. The pipe has a radius of 0.08 and a length of 0.08. The mesh of the pipe consists of 3,904 tetrahedral cells and 868 vertices within the domain, along with 740 triangular faces on the boundary.

This case presents a higher level of complexity compared to the previous one due to the discontinuous diffusion coefficient. Notably, the performance of the FNO deteriorates in the presence of irregular geometries. For the complex modes in this scenario, while FNO, DeepONet, and PI-DeepONet successfully capture the main characteristics of the solution, they fail to accurately resolve fine-scale variations, yielding MSE of  $3.68 \times 10^{-2}$ ,  $3.06 \times 10^{-2}$ , and  $4.45 \times 10^{-2}$ , respectively. The PINN struggles to converge, achieving an MSE of approximately 1.71 after 15,000 iterations. In contrast, the GreenONet framework demonstrates superior performance by effectively capturing detailed variations, underscoring its robustness and versatility in solving reaction-diffusion equations on both regular and irregular computational domains with heterogeneous diffusion coefficients.

We also analyzed the impact of BsNN and FNN architectures on the performance of the GreenONet framework. When using FNN as components, the GreenONet framework failed to achieve convergence even after 10,000 iterations, with an error of approximately  $2.24 \times 10^{-3}$ . In contrast, employing BsNN as components enabled the framework to converge to an error of  $8.13 \times 10^{-4}$  within 7,000 iterations. These results highlight the superior performance of BsNN in enhancing the efficiency and accuracy of the GreenONet framework.

Table 3: The hyper-parameters and performance of different baseline models on case of flat plane.

Model	Epochs	Learning rate	Layers	Training error	Testing error
GreensONet	7000	0.001	[6, 24, 24, 24, 1]	$8.13 \times 10^{-4}$	$8.63 \times 10^{-4}$
PINN	15000	0.001	[3, 24, 24, 24, 1]	-	1.71
DeepONet	10000	0.001	Trunk Net: [3, 24, 24, 24, 1] Branch Net 1: [ $N_{points}$ , 24, 24, 24, 1] Branch Net 2: [ $N_{points}$ , 24, 24, 24, 1]	$1.83 \times 10^{-3}$	$3.06 \times 10^{-2}$
PI-DeepONet	10000	0.001	Trunk Net: [3, 24, 24, 24, 4] Branch Net 1: [ $N_{points}$ , 24, 24, 24, 4] Branch Net 2: [ $N_{points}$ , 24, 24, 24, 4]	$4.45 \times 10^{-3}$	$4.45 \times 10^{-2}$
FNO	2000	0.001	[6, 6, 6, 6, 6, 1]	$4.18 \times 10^{-3}$	$3.68 \times 10^{-2}$

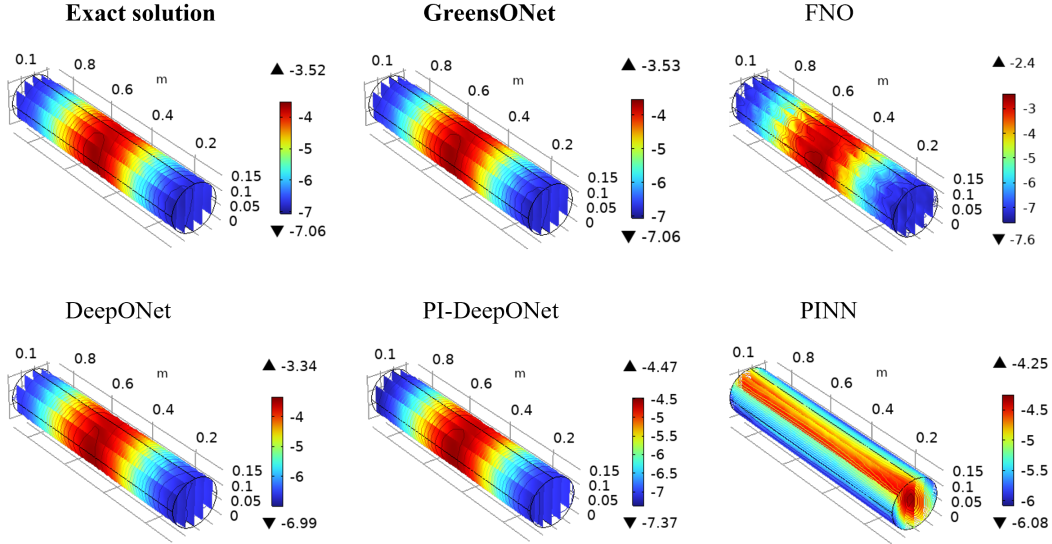


Figure 12: Case study for steady heterogeneous reaction-diffusion on flat plane: physical distribution and isotherm distribution from exact solution, and inference of GreensONet, FNO, DeepONet, PI-DeepONet, PINN (from left column to right column, from first row to second row).

### 4.3. Case 3: Stokes equations

We consider a classical benchmark problem in fluid dynamics: the 3D lid-driven cavity problem [46]. In this study, we aim to identify the matrix of Green's functions for Stokes flow [47, 36], modeled by the following system of equations over the domain  $\Omega = [0, 1]^3$ :

$$\begin{cases} \mu \nabla^2 \mathbf{u}(\mathbf{x}) - \nabla p(\mathbf{x}) = \mathbf{f}(\mathbf{x}), \\ \nabla \cdot \mathbf{u}(\mathbf{x}) = 0. \end{cases} \quad (15)$$

Here,  $\mathbf{u} = (u_x, u_y, u_z)$  denotes the fluid velocity,  $p$  represents the pressure,  $\mathbf{f} = (f_x, f_y, f_z)$  is an applied body force, and  $\mu = 1/100$  is the dynamic viscosity. As shown in Figure 13, the fluid velocity obeys no-slip boundary conditions on all walls except the top wall, where  $\mathbf{u} = (1, 0, 0)$ . The forcing term is generated using a GRF with a wavelength parameter  $\lambda = 0.1$ . Figure 13 provides an illustration of the applied body force. The mesh is uniformly discretized into tetrahedral cells, containing 1331 vertices, 6000 tetrahedral cells within the domain, and 1200 triangular faces on

the boundaries. Based on this simulation setup, we generate training and testing datasets for all models by calculating the corresponding velocity solutions ( $\mathbf{u}$ ) for various random body forces ( $\mathbf{f}$ ) using COMSOL Multiphysics <sup>®</sup>.

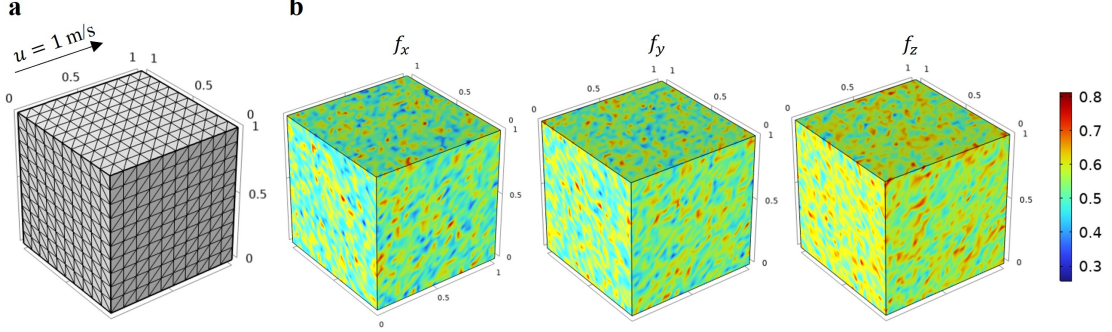


Figure 13: **a**. The simulation setting of the Stokes case; **b**. An example of the applied body force generated by GRF.

For validation, we compared our GreensONet framework against four well-known models: PINN, DeepONet, PI-DeepONet, and FNO. Table 4 and Figure 14 provide detailed comparisons between GreensONet and these baseline models. To ensure a fair evaluation, we used identical hyperparameters across all models, including training epochs, learning rate, and optimizer settings. Each model was trained for 2000 epochs with a consistent learning rate of 0.001.

GreensONet, with a five-layer architecture [6, 12, 24, 12, 1], achieved the lowest  $L_2$  error of  $5.83 \times 10^{-4}$  on the testing set. Specifically, GreensONet’s input channel consists of 6 units, accepting  $(\mathbf{x}, \xi)$  as input. For this Stokes problem, a  $3 \times 3$  network matrix was trained within GreensONet to learn the correlations between  $(u_x, u_y, u_z)$  and  $(f_x, f_y, f_z)$ , as outlined in Section 2. As shown in Figure 14 **a** and **b**, GreensONet demonstrated superior performance over PINN, DeepONet, PI-DeepONet, and FNO in calculating the velocity field for new force terms. Furthermore, Figure 14 **c** reveals that GreensONet successfully captures the primary flow characteristics of the lid-driven cavity flow, notably the large central vortex. In contrast, despite their relatively low errors, PINN, DeepONet, and PI-DeepONet fail to fully capture the vortex patterns within the cavity as effectively as GreensONet.

PINN, with a similar five-layer structure [3, 12, 24, 12, 4] to that of GreensONet, recorded an  $L_2$  error of  $1.08 \times 10^{-2}$  after 2000 epochs. Boundary constraints and PDE constraints were incorporated into the loss function as soft penalties. Specifically, the  $L_2$  error of the boundary constraint is 0.03, while the PDE loss is 1.61. In summary, while PINN offers strong interpretability, its slow convergence for high-dimensional data hinders computational efficiency, especially when recalculating for new forcing terms or boundary conditions.

DeepONet consists of a Trunk Net with layers [3, 12, 24, 12, 4] to process position information  $\mathbf{x}$ , along with two Branch Net: Branch Network 1 for handling the force term  $\mathbf{f} = (f_x, f_y, f_z)$  and Branch Network 2 for managing boundary conditions, with their layer configurations detailed in Table 4. In this setup,  $N_{points}$  denotes the total number of points in the domain, which is 1331. As shown in Table 4, DeepONet achieved an  $L_2$  error of  $2.15 \times 10^{-3}$  on the training set and  $2.17 \times 10^{-3}$  on the test set. While DeepONet shows better generalization than FNO and achieves higher accuracy than PINN, its interpretability and approximation ability remains limited.

PI-DeepONet, which includes the same Trunk Net and additional Branch Net (Branch Net 1 and Branch Net 2) as DeepONet, achieved an  $L_2$  error of  $5.31 \times 10^{-3}$ . Compared to DeepONet, PI-DeepONet has a slower convergence rate due to the additional soft constraints from partial differential equations, although its interpretability is enhanced.

As shown in Table 4, FNO achieves a very low training error ( $2.63 \times 10^{-5}$ ). However, it suffers from significant overfitting, with an MSE of  $6.86 \times 10^{-3}$  on the test set, which is high compared to other frameworks such as GreensONet, PINN, DeepONet, and PI-DeepONet. Interestingly, despite this overfitting issue, FNO is still better at capturing the vortex patterns within the cavity than PINN, DeepONet, and PI-DeepONet.

In summary, GreensONet demonstrated superior performance compared to all other models (DeepONet, PI-DeepONet, PINN, and FNO), achieving the lowest  $L_2$  error, effectively capturing critical vortex patterns, exhibiting robust generalization capability, and showcasing evident interpretability.

Table 4: The training and model hyper-parameters of different baseline models.

Model	Epochs	Learning rate	Layers	Training error	Testing error
GreensONet	2000	0.001	[6, 12, 24, 12, 1]	$5.71 \times 10^{-4}$	<b><math>5.83 \times 10^{-4}</math></b>
PINN	2000	0.001	[3, 12, 24, 12, 4]	-	$1.08 \times 10^{-2}$
DeepONet	2000	0.001	Trunk Net: [3, 12, 24, 12, 4] Branch Net 1: [ $3N_{points}$ , 12, 24, 12, 4] Branch Net 2: [ $N_{points}$ , 12, 24, 12, 4]	$2.15 \times 10^{-3}$	$2.17 \times 10^{-3}$
PI-DeepONet	2000	0.001	Trunk Net: [3, 12, 24, 12, 4] Branch Net 1: [ $3N_{points}$ , 12, 24, 12, 4] Branch Net 2: [ $N_{points}$ , 12, 24, 12, 4]	$5.59 \times 10^{-3}$	$5.31 \times 10^{-3}$
FNO	2000	0.001	[6, 20, 20, 20, 20, 3]	<b><math>2.63 \times 10^{-5}</math></b>	$6.86 \times 10^{-3}$

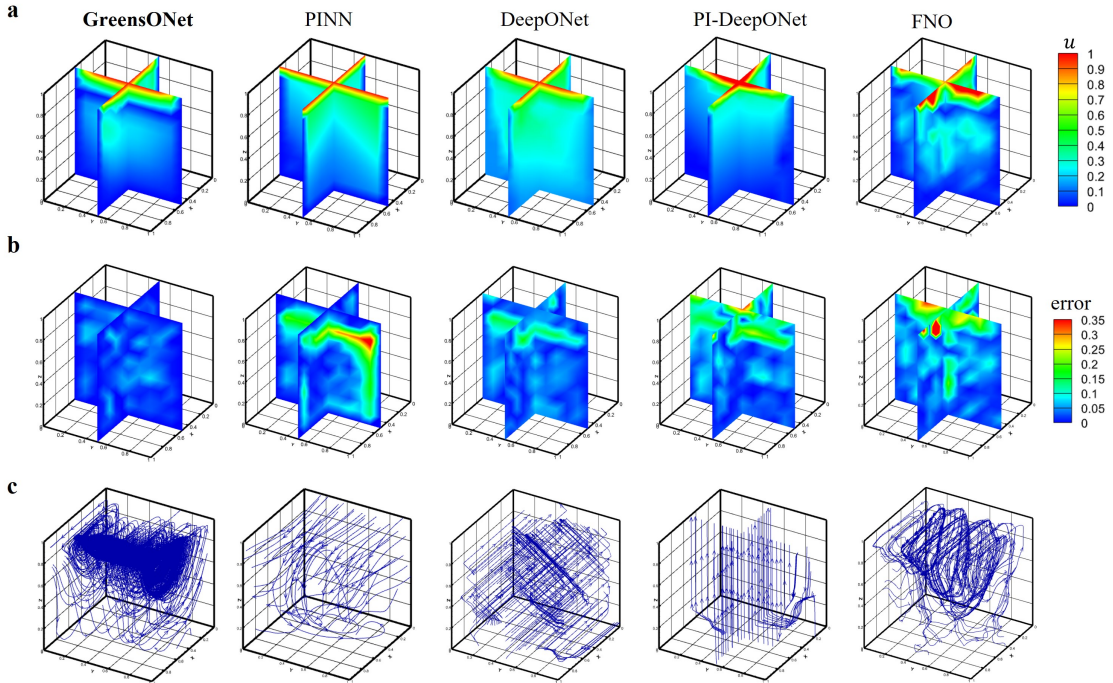


Figure 14: Case study for Stokes cavity flows: **a** velocity magnitude from inference of GreensONet, PINN, DeepONet, PI-DeepONet, FNO (from left to right); **b** Point-wise error of velocity magnitude  $(\hat{u} - u)$  by GreensONet, PINN, DeepONet, PI-DeepONet, FNO (from left to right); **c** Stream traces calculated by results of GreensONet, PINN, DeepONet, PI-DeepONet, FNO (from left to right).

## 5. Conclusions

In this work, we propose GreensONet, a novel framework inspired by Green's functions, designed to address key limitations of existing methods like PINN and DeepONet. Unlike PINN, GreensONet can directly compute new solutions for varying boundary conditions and source terms without retraining. Compared to DeepONet, GreensONet offers superior interpretability and enhanced approximation capabilities. To evaluate its performance, we conducted experiments on three classical equations: the heat equation, the reaction-diffusion equation, and the Stokes equation. These tests included scenarios with varying boundary conditions, source terms, and both homogeneous and heterogeneous setups. GreensONet consistently outperformed state-of-the-art methods, including PINN, DeepONet, PI-DeepONet, and even FNO. Interestingly, we observed that FNO performed poorly on irregular geometries, where GreensONet demonstrated robust and reliable results. The GreensONet framework provides flexibility in handling user-defined

meshes, boundary conditions, and initial conditions, making it highly accessible to engineers accustomed to traditional computational engineering simulations. This feature bridges the gap between deep learning-based solvers and conventional methods, significantly lowering the adoption barrier for CAE professionals. Looking ahead, we plan to extend GreensONet to tackle nonlinear, multiphysics coupled equations.

## Acknowledgements

This work was supported by Natural Science Foundation of Ningbo of China (No. 2023J027), China Meteorological Administration under Grant QBZ202316, the National Natural Science Foundation of China (Grant No.62106116), as well as by the High Performance Computing Centers at Eastern Institute of Technology, Ningbo, and Ningbo Institute of Digital Twin.

## References

- [1] Allan Pinkus. Approximation theory of the mlp model in neural networks. *Acta numerica*, 8:143–195, 1999.
- [2] Nicholas Perrone and Robert Kao. A general finite difference method for arbitrary meshes. *Computers & Structures*, 5(1):45–57, 1975.
- [3] Susanne C Brenner and Carsten Carstensen. Finite element methods. *Encyclopedia of computational mechanics*, 1:73–114, 2004.
- [4] Robert Eymard, Thierry Gallouët, and Raphaële Herbin. Finite volume methods. *Handbook of numerical analysis*, 7:713–1018, 2000.
- [5] Shengze Cai, Zhiping Mao, Zhicheng Wang, Minglang Yin, and George Em Karniadakis. Physics-informed neural networks (pinns) for fluid mechanics: A review. *Acta Mechanica Sinica*, 37(12):1727–1738, 2021.
- [6] Lu Lu, Pengzhan Jin, Guofei Pang, Zhongqiang Zhang, and George Em Karniadakis. Learning nonlinear operators via deepnet based on the universal approximation theorem of operators. *Nature machine intelligence*, 3(3):218–229, 2021.
- [7] Zongyi Li, Nikola Borislavov Kovachki, Kamyar Azizzadenesheli, Kaushik Bhattacharya, Andrew Stuart, Anima Anandkumar, et al. Fourier neural operator for parametric partial differential equations. In *International Conference on Learning Representations*, 2021.
- [8] Sifan Wang, Hanwen Wang, and Paris Perdikaris. Learning the solution operator of parametric partial differential equations with physics-informed deepnets. *Science advances*, 7(40):eabi8605, 2021.
- [9] Xiaowei Jin, Shengze Cai, Hui Li, and George Em Karniadakis. Nsfnets (navier-stokes flow nets): Physics-informed neural networks for the incompressible navier-stokes equations. *Journal of Computational Physics*, 426:109951, 2021.
- [10] Yuntian Chen, Dou Huang, Dongxiao Zhang, Junsheng Zeng, Nanzhe Wang, Haoran Zhang, and Jinyue Yan. Theory-guided hard constraint projection (hcp): A knowledge-based data-driven scientific machine learning method. *Journal of Computational Physics*, 445:110624, 2021.
- [11] Dashan Zhang, Yuntian Chen, and Shiyi Chen. Filtered partial differential equations: a robust surrogate constraint in physics-informed deep learning framework. *Journal of Fluid Mechanics*, 999:A40, 2024.
- [12] Aliko D Mouratidou, Georgios A Drosopoulos, and Georgios E Stavroulakis. Ensemble of physics-informed neural networks for solving plane elasticity problems with examples. *Acta Mechanica*, pages 1–20, 2024.
- [13] Peng Li, Mingliang Liu, Motaz Alfarraj, Pejman Tahmasebi, and Dario Grana. Probabilistic physics-informed neural network for seismic petrophysical inversion. *Geophysics*, 89(2):M17–M32, 2024.
- [14] Hao Xu, Yuntian Chen, Zhenzhong Zeng, Nina Li, Jian Li, and Dongxiao Zhang. Uncovering terrain-precipitation equation with interpretable ai: Towards future climate projection. *Nexus*, 2024.
- [15] Yaohua Zang, Gang Bao, Xiaojing Ye, and Haomin Zhou. Weak adversarial networks for high-dimensional partial differential equations. *Journal of Computational Physics*, 411:109409, 2020.
- [16] Maziar Raissi, Paris Perdikaris, and George E Karniadakis. Physics-informed neural networks: A deep learning framework for solving forward and inverse problems involving nonlinear partial differential equations. *Journal of Computational physics*, 378:686–707, 2019.
- [17] Bing Yu et al. The deep ritz method: a deep learning-based numerical algorithm for solving variational problems. *Communications in Mathematics and Statistics*, 6(1):1–12, 2018.
- [18] Zongyi Li, Nikola Kovachki, Kamyar Azizzadenesheli, Burigede Liu, Kaushik Bhattacharya, Andrew Stuart, and Anima Anandkumar. Fourier neural operator for parametric partial differential equations. *arXiv preprint arXiv:2010.08895*, 2020.
- [19] Zongyi Li, Nikola Kovachki, Kamyar Azizzadenesheli, Burigede Liu, Kaushik Bhattacharya, Andrew Stuart, and Anima Anandkumar. Neural operator: Graph kernel network for partial differential equations. *arXiv preprint arXiv:2003.03485*, 2020.
- [20] Ziyue Liu, Yixing Li, Jing Hu, Xinling Yu, Shinyu Shiau, Xin Ai, Zhiyu Zeng, and Zheng Zhang. Deepoheat: operator learning-based ultra-fast thermal simulation in 3d-ic design. In *2023 60th ACM/IEEE Design Automation Conference (DAC)*, pages 1–6. IEEE, 2023.
- [21] Zibo Lu, Yuanye Zhou, Yanbo Zhang, Xiaoguang Hu, Qiao Zhao, and Xuyang Hu. A fast general thermal simulation model based on multi-branch physics-informed deep operator neural network. *Physics of Fluids*, 36(3), 2024.
- [22] Ehsan Kharazmi, Zhongqiang Zhang, and George Em Karniadakis. Variational physics-informed neural networks for solving partial differential equations. *arXiv preprint arXiv:1912.00873*, 2019.
- [23] Ameya D Jagtap, Ehsan Kharazmi, and George Em Karniadakis. Conservative physics-informed neural networks on discrete domains for conservation laws: Applications to forward and inverse problems. *Computer Methods in Applied Mechanics and Engineering*, 365:113028, 2020.
- [24] Ameya D Jagtap and George Em Karniadakis. Extended physics-informed neural networks (xpinns): A generalized space-time domain decomposition based deep learning framework for nonlinear partial differential equations. *Communications in Computational Physics*, 28(5), 2020.

- [25] Ben Moseley, Andrew Markham, and Tarje Nissen-Meyer. Finite basis physics-informed neural networks (fbpinns): a scalable domain decomposition approach for solving differential equations. *Advances in Computational Mathematics*, 49(4):62, 2023.
- [26] Sifan Wang, Xinling Yu, and Paris Perdikaris. When and why pinns fail to train: A neural tangent kernel perspective. *Journal of Computational Physics*, 449:110768, 2022.
- [27] Nasim Rahaman, Aristide Baratin, Devansh Arpit, Felix Draxler, Min Lin, Fred Hamprecht, Yoshua Bengio, and Aaron Courville. On the spectral bias of neural networks. In *International conference on machine learning*, pages 5301–5310. PMLR, 2019.
- [28] Matthew Tancik, Pratul Srinivasan, Ben Mildenhall, Sara Fridovich-Keil, Nithin Raghavan, Utkarsh Singhal, Ravi Ramamoorthi, Jonathan Barron, and Ren Ng. Fourier features let networks learn high frequency functions in low dimensional domains. *Advances in neural information processing systems*, 33:7537–7547, 2020.
- [29] Hao Xu, Yuntian Chen, and Dongxiao Zhang. Worth of prior knowledge for enhancing deep learning. *Nexus*, 1(1), 2024.
- [30] Qianying Cao, Somdatta Goswami, and George Em Karniadakis. Laplace neural operator for solving differential equations. *Nature Machine Intelligence*, 6(6):631–640, 2024.
- [31] Yuhuang Meng, Jianguo Huang, and Yue Qiu. Koopman operator learning using invertible neural networks. *Journal of Computational Physics*, 501:112795, 2024.
- [32] Haixu Wu, Huakun Luo, Haowen Wang, Jianmin Wang, and Mingsheng Long. Transolver: A fast transformer solver for pdes on general geometries. *arXiv preprint arXiv:2402.02366*, 2024.
- [33] Anran Jiao, Qile Yan, Jhn Harlim, and Lu Lu. Solving forward and inverse pde problems on unknown manifolds via physics-informed neural operators. *arXiv preprint arXiv:2407.05477*, 2024.
- [34] Weiheng Zhong and Hadi Meidani. Physics-informed discretization-independent deep compositional operator network. *Computer Methods in Applied Mechanics and Engineering*, 431:117274, 2024.
- [35] Craig R Gin, Daniel E Shea, Steven L Brunton, and J Nathan Kutz. Deepgreen: deep learning of green’s functions for nonlinear boundary value problems. *Scientific reports*, 11(1):21614, 2021.
- [36] Nicolas Boullé, Christopher J Earls, and Alex Townsend. Data-driven discovery of green’s functions with human-understandable deep learning. *Scientific reports*, 12(1):4824, 2022.
- [37] Yuankai Teng, Xiaoping Zhang, Zhu Wang, and Lili Ju. Learning green’s functions of linear reaction-diffusion equations with application to fast numerical solver. In *Mathematical and Scientific Machine Learning*, pages 1–16. PMLR, 2022.
- [38] Ziad Aldirany, Régis Cottreau, Marc Laforest, and Serge Prudhomme. Operator approximation of the wave equation based on deep learning of green’s function. *Computers & Mathematics with Applications*, 159:21–30, 2024.
- [39] Nicolas Boullé, Yuji Nakatsukasa, and Alex Townsend. Rational neural networks. *Advances in neural information processing systems*, 33:14243–14253, 2020.
- [40] Pawan Negi, Maggie Cheng, Mahesh Krishnamurthy, Wenjun Ying, and Shuwang Li. Learning domain-independent green’s function for elliptic partial differential equations. *Computer Methods in Applied Mechanics and Engineering*, 421:116779, 2024.
- [41] Matthias Seeger. Gaussian processes for machine learning. *International journal of neural systems*, 14(02):69–106, 2004.
- [42] Yanjun Ma, Dianhai Yu, Tian Wu, and Haifeng Wang. PaddlePaddle: An open-source deep learning platform from industrial practice. *Frontiers of Data and Computing*, 1(1):105–115, 2019.
- [43] Nicolas Boullé and Alex Townsend. Learning elliptic partial differential equations with randomized linear algebra. *Foundations of Computational Mathematics*, 23(2):709–739, 2023.
- [44] Yanzhi Liu, Ruifan Wu, and Ying Jiang. Binary structured physics-informed neural networks for solving equations with rapidly changing solutions. *arXiv preprint arXiv:2401.12806*, 2024.
- [45] Robert A Jacobs, Michael I Jordan, Steven J Nowlan, and Geoffrey E Hinton. Adaptive mixtures of local experts. *Neural computation*, 3(1):79–87, 1991.
- [46] Howard C Elman, David J Silvester, and Andrew J Wathen. *Finite elements and fast iterative solvers: with applications in incompressible fluid dynamics*. Oxford university press, 2014.
- [47] John R Blake. A note on the image system for a stokeslet in a no-slip boundary. In *Mathematical Proceedings of the Cambridge Philosophical Society*, volume 70, pages 303–310. Cambridge University Press, 1971.